Nanoscale

PAPER

View Article Online
View Journal | View Issue

Cite this: *Nanoscale*, 2019, **11**, 1827

Facet-regulated adhesion of double-stranded DNA on palladium surfaces†

Zonglin Gu,‡[a] Lin Zhao,‡[a] Cuicui Ge,‡[a] Shengtang Liu,[a] Ge Fang,[a] Serena S. Chen,[b] Zaixing Yang*[a] and Ruhong Zhou*[a,b,c]

Received 1st August 2018,
Accepted 18th December 2018

DOI: 10.1039/c8nr06203j

rsc.li/nanoscale

A better understanding of interactions between metal–nanomaterial surfaces and biomolecules such as DNAs is critical for their biomedical applications. Here we investigated double-stranded DNA (dsDNA) adhering to palladium (Pd) nanosheets with two different exposed facets, {100} and {111}, using a combined computational and experimental approach. Different dsDNA binding modes on the two surfaces were observed, with a surprising "upright" conformation on Pd(100) and a "flat" conformation on Pd(111). Molecular dynamics simulations showed a stronger binding of the dsDNA on Pd(111) than Pd(100), which resulted in significant conformational changes and hydrogen bond breakage in the dsDNA on Pd(111). Further analyses revealed that the different binding strengths were caused by the number and arrangement of water molecules in the first solvation shell (FSS) of the two Pd surfaces. The water hydrogen bond network in the FSS of Pd(100) is compact and resists the embedding of dsDNA, while it is less compact on Pd(111), which allows penetration of dsDNA and its direct contact with Pd(111) surface atoms, thereby exhibiting stronger binding. Further free energy calculations with umbrella sampling supported these observations. Finally, these computational predictions on the adsorption capacity of dsDNA on Pd surfaces were confirmed by gel electrophoresis experiments.

Introduction

As nanomaterials are being extensively used in biomedical research, bio–nano interfaces have been attracting ever increasing interest, particularly in the fields of materials engineering and nanotoxicology. It is necessary to understand the molecular mechanisms of bio–nano interactions at their interfaces, which are especially important for applications in biomedicine, such as drug delivery,[1] bio-sensing,[2–4] optical imaging,[5] and nanotherapeutics.[6–8] Many experimental techniques have been applied to measure these bio–nano interactions at the molecular level. However, even with the most state-of-the-art experimental techniques currently available, it is still very challenging to monitor the dynamics of these bio–nano interactions at the subnanosecond timescale and/or to elucidate the interfacial structural details at the subnanometer length scale. To this end, molecular dynamics (MD) simulations are widely used to investigate bio–nano interactions at different time and length scales.[9–11] A combined experimental and computational approach is thus in high demand to provide a more comprehensive understanding of the properties of these nanomaterials at bio–nano interfaces. Taking graphene for example, the experiments demonstrated that graphene possesses antibacterial activity against *Escherichia coli*. It was revealed by the MD simulations that the activity is due to the insertion of graphene into the bacterial cell membranes in which graphene extracts the phospholipids by dispersion forces.[12] Another example is graphene oxide (GO) for lipase stabilization and activation. GO was experimentally demonstrated as a platform engineered for lipase immobilization with enhanced catalytic activity. The computational results further verified the underlying molecular mechanisms (by opening up the lids) and the binding characteristics of lipase on graphene oxide surfaces.[13] GO was also engineered to couple with fluorescent single-stranded DNA (ssDNA) probes for detection of the target DNA based on a large discrepancy in the interactions of ssDNA and dsDNA with GO. MD simulations demonstrated that the stronger interaction between ssDNA and GO is induced by π-attraction.[14]

Meanwhile, palladium (Pd) nanoparticles, with a distinctive surface morphology and physicochemical properties,[15] have been used for many biological applications. For example, the

[a]*State Key Laboratory of Radiation Medicine and Protection, School for Radiological and Interdisciplinary Sciences (RAD-X), and Collaborative Innovation Center of Radiation Medicine of Jiangsu Higher Education Institutions, Soochow University, Suzhou 215123, China. E-mail: zxyang@suda.edu.cn*
[b]*IBM Thomas J. Watson Research Center, Yorktown Heights, NY 10598, USA. E-mail: ruhongz@us.ibm.com*
[c]*Department of Chemistry, Columbia University, New York, NY 10027, USA*
†Electronic supplementary information (ESI) available. See DOI: 10.1039/c8nr06203j
‡These authors contributed equally.

gold-overbranched Pd nanostructure has shown effective photothermal hyperthermia in cancer therapy with both *in vitro* and *in vivo* experiments.[16] More importantly, with some facet control, unalloyed Pd nanocrystals can be designed for cancer therapy through manipulating variant molecular oxygen ($^1O_2$) activation on different facets.[17] On the other hand, fine-scale Pd nanoparticles have been found to have antimicrobial activities against Gram-negative *Escherichia coli* and Gram-positive *Staphylococcus aureus*.[18] Despite extensive biological applications of Pd nanoparticles, their direct interactions with biomolecules at various interfaces have not been fully understood. It has been previously reported that peptides have enhanced adsorption capacity on Pd(111) as compared to Pd(100).[19] In this study, we use a combination of computational and experimental methods to examine the difference in the binding strength and adsorption capacity of another essential biomolecule, dsDNA, on both Pd(100) and Pd(111) surfaces. We aimed to understand the interactions between a dsDNA and Pd facets at the molecular level and the corresponding differential structural effects on the dsDNA. Our findings provide new insights into the future design of metal nanostructures for biomedical applications.

Results

The Pd sheets with two different facets, which reflect different atomic arrangements, were constructed as shown in Fig. 1a and b. The unit cells were square and rhombus for the {100} and {111} facets, respectively. The distance between two adjacent surficial Pd atoms was 2.75 Å in both sheets. Moreover, the atomic arrangement of Pd(111) was more compact than that of Pd(100). The initial system is depicted in Fig. 1c, wherein the dsDNA was placed parallel to the *z*-axis above the Pd sheets (see the Methods section for more details). Three independent simulations were performed for each system. Each simulation lasted for 500 ns. Fig. 2 illustrates the different binding modes of the dsDNA on the two Pd facets and the number of atoms that were in contact over the course of the simulations. The dsDNA "lay-down" (*i.e.* "flat") on the Pd(111) surface in all three simulations, whereas the dsDNA "stood-up" (*i.e.*, "upright)" on Pd(100) in one simulation and tilted slightly on Pd(100) in the other two simulations. The different binding modes suggested that the binding affinity of Pd(111) for the dsDNA is stronger than that of Pd(100). The bias in the binding strength (or adsorption capacity) of the dsDNA favoring Pd(111) was also reflected in the average number of atoms in contact with the Pd surfaces. There were 332.3 ± 5.1, 320.1 ± 4.0, and 362.4 ± 4.3 atoms on average that were in contact with Pd(111) at the end of the three 500 ns MD trajectories, whereas there were only 69.7 ± 2.9, 162.9 ± 6.0, and 83.3 ± 4.6 atoms that were in contact with Pd(100) at the end of the equivalent simulations. Moreover, the binding energy of the dsDNA to Pd(111) was 2.5 to 6.4 times stronger than that to Pd(100), but the strong binding to Pd(111) caused severe damage to the dsDNA, resulting in the conformational change and hydrogen bond breakage (Table 1). The root mean square deviation (RMSD) values of the dsDNA on Pd(111) reached 10.0 Å, whereas they were less than 4.5 Å on Pd(100). Furthermore, the number of hydrogen bonds within the dsDNA decreased 24.50% to 47.08% in Pd(111)–dsDNA, indicating a partial denaturation of the dsDNA. Based on the above analyses, Pd(111) showed a stronger binding to the dsDNA than Pd(100), with a higher denaturation capability to dsDNA as well. Table 1 summarizes the binding energies of the dsDNA to the two Pd surfaces and the changes in the dsDNA structure in Pd(100)–dsDNA and Pd(111)–dsDNA trajectories. To verify whether the binding processes of dsDNA onto the Pt(111) surface had converged, one trajectory was further extended to 700 ns (Fig. S1†). During the extended time interval from 500 ns to 700 ns, the contact number remained approximately at a constant (~329.0 ± 8.0), and no further significant structural changes of dsDNA were observed, suggesting an overall convergence of the binding process.

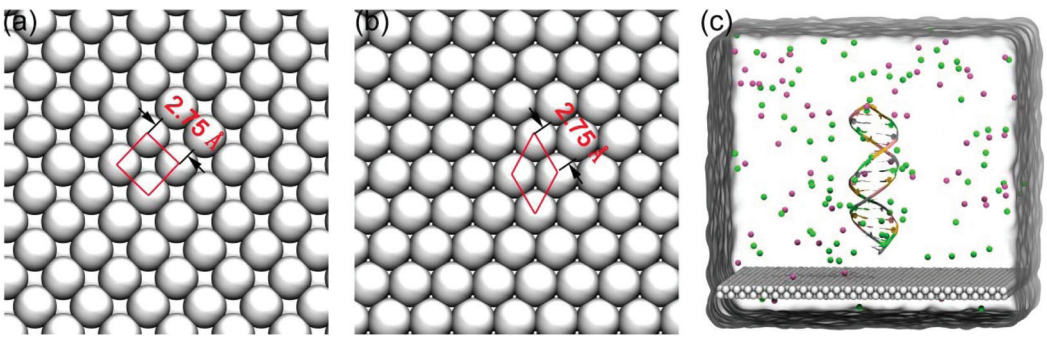

Fig. 1 Models of the two Pd sheets and an initial system for the simulations. The (a) Pd(100) sheet model and (b) the Pd(111) sheet model. The red quadrangles represent the unit cells of the two facets. The distance between neighboring Pd atoms is 2.75 Å. (c) An initial system for the simulations performed in this study. The Pd atoms are shown in white spheres. The K^+ and Cl^- ions are displayed in green and purples spheres, respectively. The dsDNA is presented in ribbon mode. Water is rendered transparently, and the water surface shows the boundaries of the periodic cell. In this study, two systems, Pd(100)–dsDNA and Pd(111)–dsDNA, were constructed, each of which had the dsDNA placed parallel to the *z*-axis above the corresponding Pd sheet.

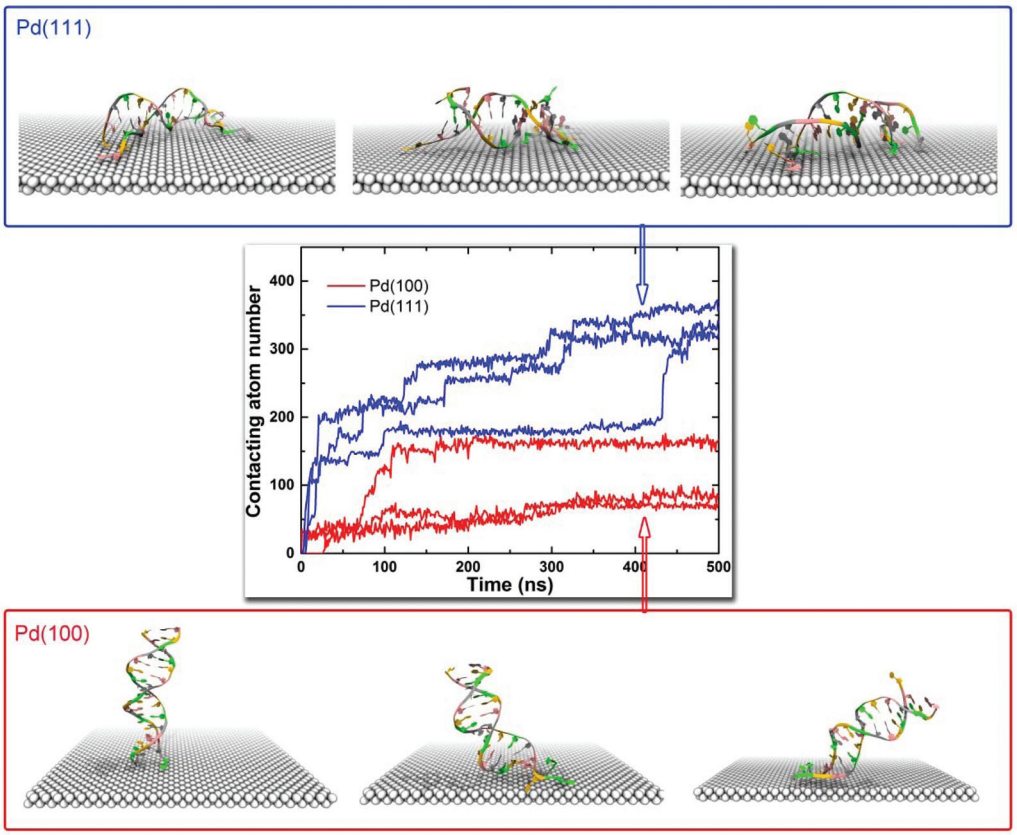

Fig. 2 Distinct adsorption behaviors of the dsDNA on the two Pd surfaces. The in-between plot shows changes in the number of atoms that were in contact between the dsDNA and the two Pd surfaces in the six MD trajectories. The snapshots in the blue frame are the final structures of the three Pd(111)–dsDNA trajectories, while the ones in the red frame are the final structures of the three Pd(100)–dsDNA trajectories.

Table 1 A comparison of Pd(100)–dsDNA and Pd(111)–dsDNA on the binding energies of the dsDNA to the two Pd sheets, the root mean square deviation (RMSD) values of the dsDNA, and the numbers of remaining hydrogen bonds in the dsDNA shown in percentages (H-bond ratio). All data were calculated from the last 30 ns of the corresponding MD trajectory

	Pd(100)–dsDNA			Pd(111)–dsDNA		
Binding energy (kcal mol^{-1})	−144.15 ± 2.73	−301.82 ± 4.72	−154.93 ± 3.68	−746.43 ± 10.07	−792.95 ± 7.30	−924.87 ± 8.23
RMSD (Å)	3.0 ± 0.5	4.5 ± 0.4	3.6 ± 0.5	6.9 ± 0.1	10.0 ± 0.1	6.0 ± 0.1
H-Bond ratio (%)	91.40 ± 4.18	82.41 ± 3.61	86.56 ± 4.59	75.50 ± 4.69	59.60 ± 4.50	52.92 ± 4.26

It was noteworthy that the heavy atom contact number of dsDNA onto the Pd(111) surface showed a very clear step-wise pattern. To better understand this dynamical process, binding snapshots at key time points were further examined (Fig. S2†). In general, the relative smaller jumps such as at the time points of t = 10, 23, 60, 102, and 467 ns were induced by the sudden adsorption of a single nucleobase, while the largest jump at t = 338 ns (with the contact number sharply increased from ~185 to ~300) was due to the fact that dsDNA completely lay down (flat) onto the Pd(111) surface. Interestingly, during the adsorption process of the dsDNA onto the Pd(111) surface, we found an approximate linear relationship between the direct dsDNA–Pd(111) interaction energy and the dsDNA–Pd(111) tilt angle (Fig. S3;† here, the dsDNA–Pd(111)/Pd(100) tilt angle was defined as the angle between the axial direction of the dsDNA and the tangential direction of the Pd surface). More specifically, the smaller the tilt angle, the larger the energy, which strongly suggests that it is energetically more favorable for the dsDNA to completely lie down on the Pd(111) surface (Fig. S3†). On the other hand, in the case of Pd(100), the dsDNA–Pd(100) interaction energy and the dsDNA–Pd(100) tilt angle did not show any obvious correlations. These results implied two distinct dsDNA binding patterns for the two Pd sheets.

To further examine the difference in the binding of the dsDNA to Pd(100) and Pd(111) at the interfaces, we highlighted the key binding deoxyribonucleosides in two representative trajectories shown in Fig. 3. Fig. 3a shows the first two deoxyribo-

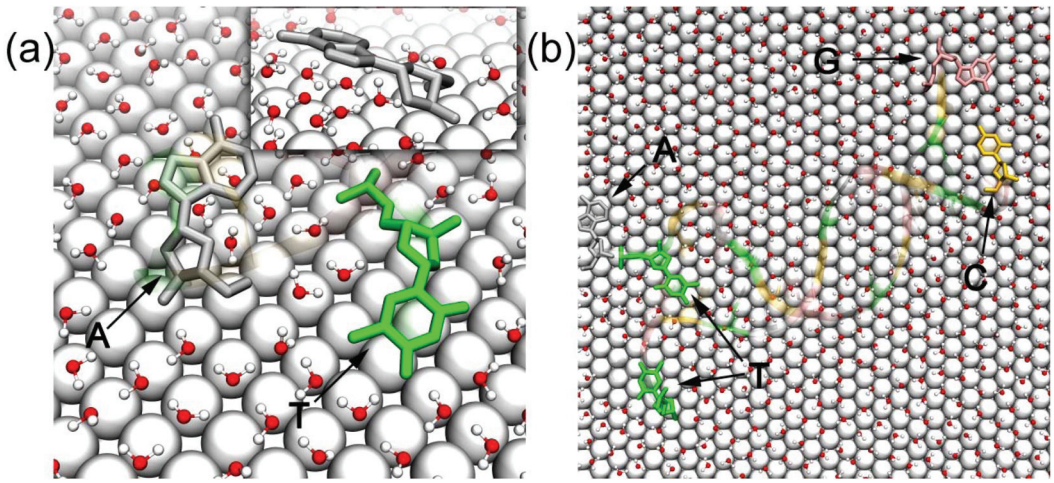

Fig. 3 Difference in the binding of the dsDNA to the two Pd surfaces at the interfaces. The key binding deoxyribonucleosides are labelled and shown in stick mode. A snapshot was taken from the last structure of one of the three Pd(100)–dsDNA trajectories (a) or from that of the three Pd(111)–dsDNA trajectories (b). The water molecules in the FSS are displayed in ball-and-stick mode, wherein the oxygen atoms are colored in red and the hydrogen atoms in white. The embedded figure in (a) is a highlight of the binding mode of the deoxyadenosine.

nucleosides (A and T) touching the surface of Pd(100) and the water molecules in the first solvation shell (FSS). The first nucleoside T also lay down on the Pd(100) surface and was surrounded by a large amount of water molecules, whereas the second nucleoside A bound to the surface through the deoxyribose with a tilted orientation (*i.e.*, suspended in the solvent, as shown in the embedded subfigure). The binding mode of the dsDNA is completely different on the Pd(111) surface, wherein all deoxyribonucleosides completely lay down on the surface with a face-to-face flat configuration (Fig. 3b), which is considered the most stable interaction pattern.[20–22]

To further explore the underlying molecular mechanism of the difference in the adsorption capacities of the dsDNA on the Pd(100) and Pd(111) surfaces, we analyzed the number density of water molecules and hydrogen-bond networks on the two surfaces (Fig. 4). The FSS of Pd(100) was slightly closer to the Pd surface than that of Pd(111), wherein the distances were at 0.24 and 0.26 nm from the Pd(100) and Pd(111) surfaces, respectively. Moreover, the maximum number of water molecules on Pd(100) was 545.89 nm^{-3}, which was higher than that on Pd(111) (496.21 nm^{-3}). We further assessed the compactness of the hydrogen bond network in the first solvation shell (FSS) of the two Pd surfaces by computing the average number of hydrogen bonds that each water molecule can form with other water molecules within the FSS. The number was ~3.5 for Pd(100) and ~2.8 for Pd(111), indicating a less compact hydrogen bond network in the FSS of Pd(111). Meanwhile, we also compared the water binding energy in the FSS to the two Pd surfaces (Fig. S4†). The water binding energies were about −6.97 kJ mol^{-1} and −4.92 kJ mol^{-1} for the Pd(100) and Pd(111) surfaces, respectively, suggesting that a water molecule within the FSS hydrogen-bond network of Pd(111) was less energetically favorable due to the relatively sparser hydrogen-bond network. Furthermore, the hydrogen-bond networks and water density maps in the FSS demonstrated different distributions of water molecules on the two surfaces (Fig. 4c–f). As Pd atoms are arranged differently on the {100} and {111} facets, the water molecules followed accordingly in the two FSS, resulting in different DNA binding patterns and affinities on Pd(100) and Pd(111). The water molecules in the FSS of Pd(100) were located exclusively at the uncovered gaps between four Pd atoms, forming a very compact and dense hydrogen-bond network, which prevented the dsDNA from binding and resulted in a lower binding affinity. The water molecules in the FSS of Pd(111), on the other hand, had less compact density at the gaps between three Pd atoms due to the tight packing of atoms in Pd(111) on their own. The loose network of hydrogen bonds in the FSS of Pd(111) allowed more interactions between the Pd atoms and the dsDNA and thus increased the binding. In fact, the relatively more ordered and compact hydrogen-bond network within the FSS of the {100} facet over the {111} facet was also observed in other metal nanosheets, such as Pt(100) and Au(100), and independent of the force fields used (no matter the fixed-charge or polarizable force fields).[23,24] This robust phenomenon was mainly due to the much better match between the lattice constants of {100} facets and the inherent geometry of the water hydrogen-network within the FSS.[23,24]

To quantify the binding affinities of dsNDA on both Pd(100) and Pd(111), we calculated the potential of mean force (PMF) values of deoxyadenosine (A) along the *z*-direction of the two Pd nanosheets. As shown in Fig. 5a, the free energy profile of the deoxyadenosine adsorption on the Pd(100) surface featured two minima, labeled as (i) and (ii), locating at the positions of the second solvation shell (SSS) and the first solvation shell (FSS), with ΔG_i = −27.7 kJ mol^{-1} and ΔG_{ii} = −28.3 kJ mol^{-1}, respectively. Note that there was a large free energy barrier between the minima (i) and (ii) (deoxyadenosine

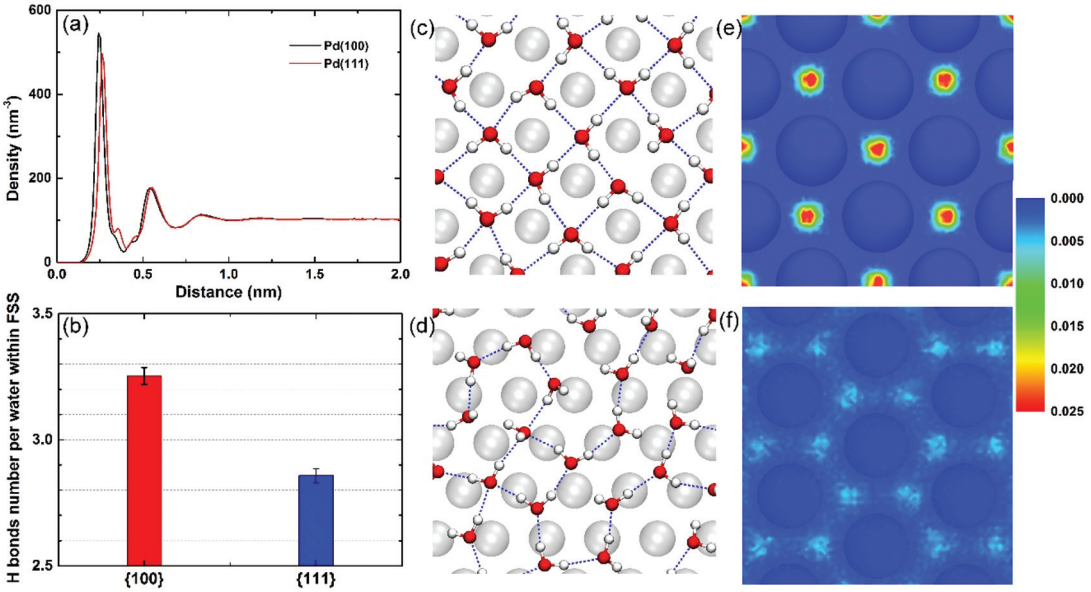

Fig. 4 Number density of water molecules and hydrogen-bond networks on Pd(100) and Pd(111). (a) Number density of water molecules along the *z*-direction of the Pd plane, where the outermost Pd layer is set at $z = 0$. (b) The average number of hydrogen bonds that each water molecule in the FSS of the two Pd surfaces formed. (c) Hydrogen-bond network in the FSS of Pd(100). The blue dashed lines represent hydrogen bonds. (d) Hydrogen-bond network in the FSS of Pd(111). (e) Water density map in the FSS of Pd(100). (f) Water density map in the FSS of Pd(111).

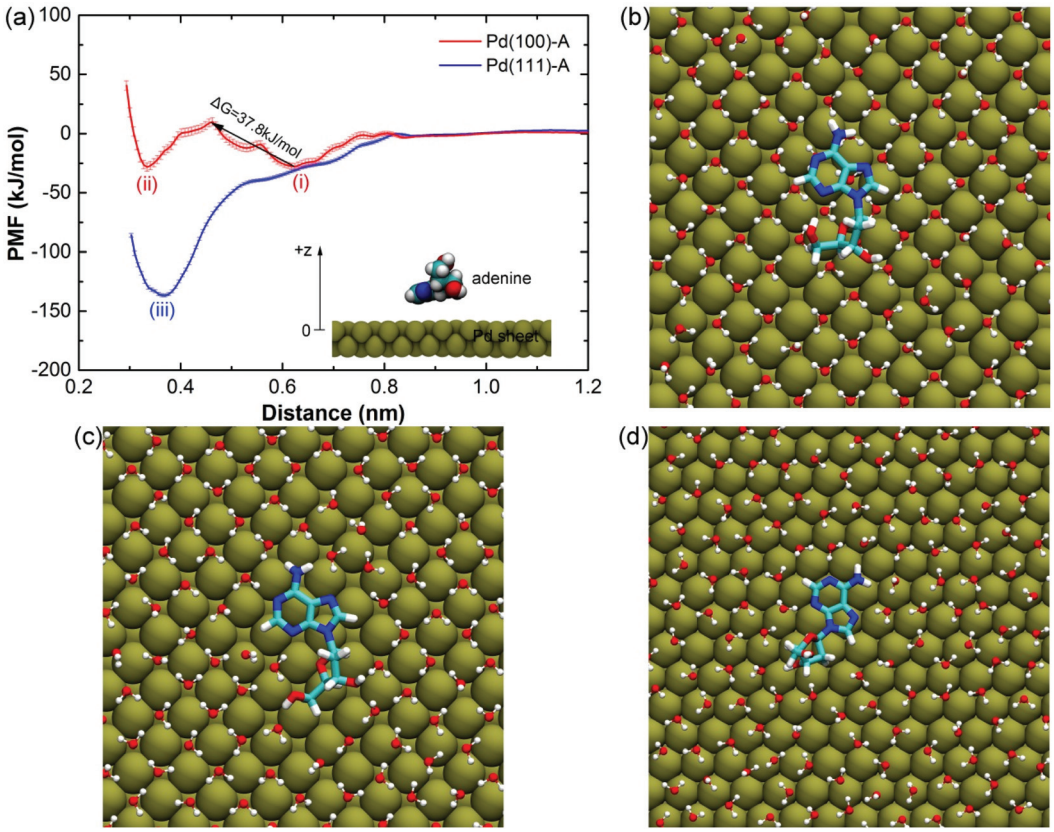

Fig. 5 Potential of mean force (PMF) of deoxyadenosine moving along the *z*-direction of Pd(100) (red curve) and Pd(111) (blue curve), with binding conformations at the corresponding potential wells. (a) The PMF curves show the deoxyadenosine (adenine) binding free energy on Pd(100) and Pd(111), respectively. The embedded figure represents the position of the deoxyadenosine relative to a Pd sheet. The *z* coordinate of the upper Pd atomic layer is set to zero. (b–d) The conformations of deoxyadenosine binding to Pd(100) and Pd(111) surfaces correspond to the potential wells of position (i), (ii) and (iii).

moving from the Pd(100) SSS toward the FSS) of 37.8 kJ mol^{-1}, which was likely inaccessible at room temperature (~15 kT at room temperature). This distinctive free energy barrier is ascribed to the unique Pd(100) facet topology, which regulates and forms a unique FSS hydrogen bond network, as illustrated in Fig. 4 above. When the deoxyadenosine approaches the Pd(100) surface, *i.e.* moving from (i) to (ii) (Fig. 5b and c), this deoxyadenosine needs to break this compact hydrogen bond network and simultaneously dehydrate partially (see Fig. 5c). This is because the deoxyadenosine cannot form an equal number of hydrogen bonds with neighboring interfacial water molecules due to the unique surface facet of Pd(100), with its interfacial water molecules reorganized to form a new compact water network but not in close contact with deoxyadenosine (Fig. 5c). Thus, this partial dehydration penalty of deoxyadenosine results in a weaker binding to the Pd(100) surface, even if breaking through the FSS, with a binding free energy of ΔG_{ii} = −28.3 kJ mol^{-1} only. On the other hand, for Pd(111), there was no obvious energy barrier when deoxyadenosine moves from the Pd(111) SSS to FSS, implying that the deoxyadenosine can freely adsorb onto the Pd(111) surface without any free energy cost and that the deoxyadenosine can equally replace the unordered water molecules of the FSS on Pd(111) (Fig. 5d), *i.e.*, no dehydration penalty, thus resulting in a significantly stronger binding free energy of ΔG_{iii} = −136.6 kJ mol^{-1}. To make this point clearer, we repeated the PMF calculations for the same deoxyadenosine on both Pd(100) and Pd(111) without water (*i.e.* in the gas phase); the PMF potential wells are very comparable as shown in Fig. S5,† as expected. Similarly, the direct interaction energies between the Pd sheets and deoxyadenosine at position (ii) and (iii) were also similar as shown in Table S2.† Therefore, it is the compact water hydrogen bond network and potential partial dehydration of dsDNA on the Pd(100) surface that result in surprising differences in binding affinities and binding patterns on Pd(100) *versus* Pd(111). In other words, the stronger adsorption between Pt(111) and dsDNA was contributed by the less compact water hydrogen-bond network and stronger direct dispersion interactions (*i.e.* the direct face-to-face binding pattern).

Moreover, the potential influences of a salt solution on the subtle binding between dsDNA and two Pd facets were also investigated. To address this, we also studied the binding behaviors of ions onto two Pd facets (Fig. S6†). In general, more ions accumulated on the Pd(111) surface than on Pd(100) due to the weaker resistance of the less compact FSS of the Pd{111} facet. Moreover, Cl^- was more likely to intrude into the FSS of the two facets than Na^+. The key reason was that Cl^- could reside in the hollow sites among four Pd atoms and be further stabilized by four neighboring water molecules due to favorable electrostatic attraction. More importantly, we observed that Cl^- accommodation cannot significantly reduce the order of the original highly uniform rhombic water hydrogen-bond network within the FSS of Pd(100). That is to say, the invasion of ions did not significantly affect the regulatory role of the compact water hydrogen-bond network in the FSS of {100} facets in the dsDNA adsorption. Therefore, we can conclude that the impact of ions on the binding behavior of dsDNA to the two Pd facets is relatively small.

It was also noteworthy that both the fixed-charge and polarizable force fields were widely used in the study of bio–metal substrate interactions. The polarizable force fields often possessed more advantages in describing the charge properties, which might be somewhat underestimated in the fixed-charge force fields. Having said that, usages of different force fields have led to many common conclusions, *i.e.* biomolecules had stronger binding capacity to the {111} facet than to the {100} facet. For instance, using the GolP-CHARMM polarization force field, a peptide was found to have stronger binding affinity onto Au(111) than Au(100).[24,25] Recent research conducted by Heinz and co-workers developed a set of simple polarizable force fields of Au nanostructures that includes a Lennard-Jones potential and a harmonically coupled core–shell charge pair for every Au atom. They verified that a peptide (sequence: DYKDDDDK) showed a stronger binding energy on the Au(111) surface than on Au(100), where the FSS on Au(100) hindered the direct contact of the peptide with Au(100).[26] Meanwhile, a similar result was also reported in the protein–Ag interaction when using a polarization force field (AgP-CHARMM FF) to model Ag flakes.[27] On the other hand, using the fixed-charge force fields, some other studies have also found that peptides demonstrated much stronger adsorption capacity on the {111} facet over the {100} facet of both Au and Pd nanostructures.[19,28] Taken together, the stronger biomolecules adsorbing affinity of the {111} facet than the {100} facet was very robust and independent of the force fields used for metal atoms.

To further verify our predictions in the MD simulations, we synthesized the Pd nanocrystals with {100} (cubic) and {111} (octahedral) facets using the same methods as described previously.[17,29] The facets and geometries of the Pd nanocrystals were characterized by transmission electron microscopy (TEM) and high-resolution TEM (HRTEM). Fig. 6a and b show the representative TEM images. The synthesized Pd nanocrystals have cubic or octahedral shapes with an average length of 10 nm. HRTEM analyses with the corresponding Fast Fourier Transform (FFT) patterns taken from single nanocrystals indicated that Pd cubes and octahedra were enclosed by {100} and {111} facets, respectively (Fig. 6c and d). Using the above Pd nanocrystals, we measured the adsorption capacity of a dsDNA, a complementary DNA (cDNA), and obtained the amount of the adsorbed cDNA through agarose gel electrophoresis. The results are shown in Fig. 6e and f. Agarose gel electrophoresis experiments revealed a larger amount of cDNA in the supernatant of the sample with Pd(100) than with Pd(111). Under the same experimental conditions, Pd(111) adsorbed about 26.97% of the cDNA, whereas Pd(100) only about 11.11%, which supported our theoretical prediction that Pd(111) possesses a higher binding affinity for dsDNA than Pd (100). Thus, both our experimental and theoretical results confirmed that different Pd facets can have different adsorption capacities of the dsDNA, with Pd(111) showing a higher capacity than Pd(100).

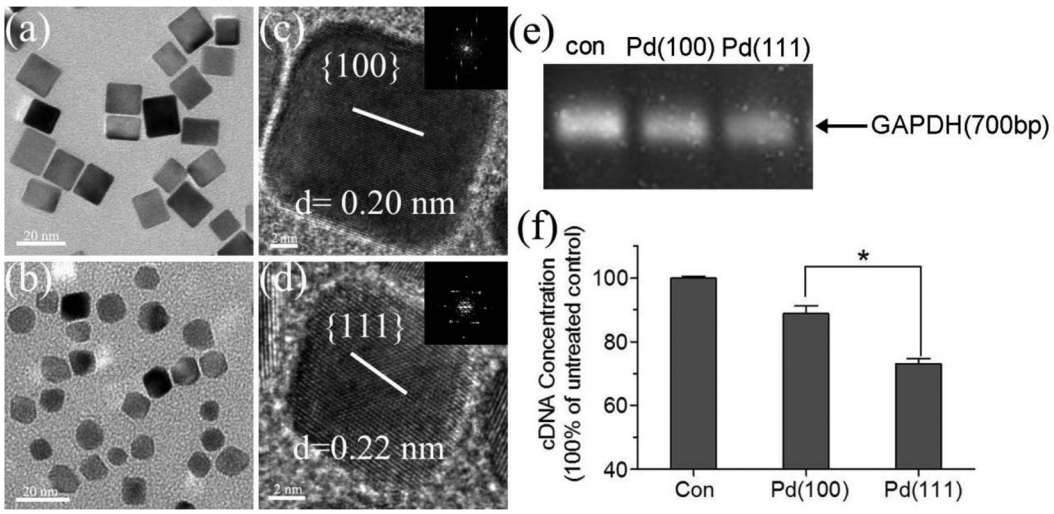

Fig. 6 TEM images of the synthesized Pd nanocrystals and the adsorption capability test of the cDNA on Pd(100) and on Pd(111) measured by agarose gel electrophoresis. (a, b) Transmission electron microscopy (TEM) images of the Pd nanocrystals. (c, d) High-resolution TEM (HRTEM) images and the Fast Fourier Transform (FFT) patterns of the Pd nanocrystals. (e) Gel image showing the amount of cDNA in the supernatants after treatment with Pd(100) or with Pd(111). The first lane is the control (con). (f) cDNA concentration after treatment with Pd(100) or with Pd(111). Around 26.97% of the cDNA adsorbed on Pd(111), and 11.11% of that adsorbed on Pd(100) (*$P < 0.05$).

Conclusion

We investigated the molecular mechanisms of dsDNA binding to two Pd surfaces with different facets, {100} and {111}, using MD simulations, PMF calculations and agarose gel electrophoresis assays. Our simulation results revealed that the dsDNA adhered to the two surfaces with surprisingly different binding modes and strengths, with Pd(111) being significantly more favored than Pd(100). The binding on Pd(111) is so strong that it can also cause the dsDNA to partially denature. We further showed that the different binding modes of the dsDNA resulted from different arrangements of the water molecules in the FSS on the two surfaces. The hydrogen bond network is more compact on Pd(100), which makes the Pd(100) surface less accessible to the dsDNA, with a well-formed single water layer in-between. The PMF free energy profiles and agarose gel electrophoresis assays further confirmed the stronger binding and higher adsorptive capacity of dsDNA on Pd(111) than on Pd(100).

On the other hand, in a realistic and more complicated biological environment, one important issue regarding the nanomaterial–biomolecule interaction is the competitive binding among different biomolecules with the nanomaterial surfaces. This important concept was originally proposed by Dawson and co-workers, and has been studied by many researchers.[30–32] Whereas, it should be noted that it is the direct interacting mechanisms between biomolecules and the bare nanomaterial surface, which have been proved to be heavily mediated by nanomaterials' surficial properties, that establish the molecular bases for the subsequent competitive biomolecules' binding behaviors.[33] Given that the surface properties of different nanomaterials can vary considerably, the interaction mechanisms between different nanomaterials and the same biomolecules can also vary greatly. In other broad applications, the growing usages of biomolecules (including, DNA and peptide) in guiding the programmable synthesis of sophisticated metal nanocrystals of specific facets also highlighted the importance of the pure bio–nano binding.[34–40] Unfortunately, the related information was still relatively insufficient. For instance, in this study, the revealed distinct interacting mechanisms for DNA with two different Pd facets remained unclear to date. Our current findings might have provided new insights into the future design of metal nanostructures for biomedical applications.

Methods

Molecular dynamics simulations

Both palladium (Pd) sheets were constructed in two atomic layers as displayed in Fig. 1(a) and (b). The Pd(100) and Pd(111) models consisted of 2704 and 2880 atoms with surface dimensions of 10.11×10.11 nm^2 and 9.90×9.53 nm^2, respectively. A B-form double-stranded DNA (dsDNA) model (sequence: ATCGATCGATCGATCG) was generated from the http://structure.usc.edu/make-na/server.html server, which was similar to our previous work.[41] The dsDNA was placed parallel to the z-axis above the Pd sheets with a minimum distance of 12 Å as shown in Fig. 1(c) (defined as Pd(100)–dsDNA and Pd(111)–dsDNA systems). The two systems were solvated and ionized with 0.15 M KCl to mimic physiological environments. In addition, another two systems with the Pd sheets and water molecules were constructed to probe the hydrogen bond networks on the two surfaces (defined as Pd(100)–water and Pd(111)–water systems). More simulation details can be found in Table S1.† These four systems served

as the initial structures for the molecular dynamics simulations.

The simulations were carried out using the GROMACS software package (version 4.6.6)[42] with the CHARMM27 force fields[43,44] (the force fields of Pd atoms were obtained from a previous study[45]). The VMD software[46] was used to analyze and visualize the simulation results. The TIP3P water model[47] was used for water molecules. The temperature was maintained at 300 K using a v-rescale thermostat[48] and pressure was kept at 1 atm by applying a Berendsen barostat[49] (only applied in the *z*-direction of the simulation box). The Pd sheets were fixed throughout the simulations. The long-range electrostatic interactions were treated with the PME method,[50,51] and the van der Waals (vdW) interactions were calculated with a cutoff distance of 1.0 nm. All solute bonds (bond stretch) were constrained at their equilibrium values with the LINCS algorithm,[52,53] which was also applied elsewhere regarding biomolecules,[54–56] though only the bonds with H-atoms were constrained in many other relevant studies[57–59] as well. The geometry of water was constrained by using the SETTLE algorithm.[60] A time step of 2.0 fs was used in the production runs.

Potential of mean force (PMF)

The PMF values of deoxyadenosine (or a water molecule) along the *z*-direction of the Pd(100) and Pd(111) surfaces were calculated using umbrella sampling simulations.[61–63] The distance (d) to the Pd surface was restrained at a reference distance (d_0) with a harmonic force

$$F = k \times (d - d_0)$$

where k is the force constant (ranging from 2000 to 20 000 kJ mol^{-1} nm^{-2}). The spacing of the sampling windows was 0.05 nm. At each d_0, the system was equilibrated for 2 ns before a 10 ns productive run. The free energy profiles were obtained by using the g_wham tool that implements the Weighted Histogram Analysis Method.[64–66]

Agarose gel electrophoresis

To measure the binding affinities of Pd(100) and Pd(111) to DNA, we prepared a cDNA from A549 cells (obtained from the American Type Culture Collection, Rockville, MD). All the RNA in the cells was extracted using the TRIzol reagent (Invitrogen, USA). Then, the cDNA was generated from 500 ng of RNA using a reverse transcriptase (Invitrogen, USA). The PCR primers were as follows: GAPDH sense, 50-CAACTACATGGTCT-ACATGTTCC-30, antisense, 50-CAACCTGGTCCTCAGTGTAG-30. The reaction conditions of PCR and cycle numbers were rigorously adjusted so that each reaction occurred within the linear range of amplification. The detailed methods for GAPDH cDNA synthesis have been described previously.[67] Pd(100) and Pd(111) were added to the cDNA at a 1 : 1 concentration ratio. The cDNA sample without adding a Pd sheet served as a control. After 24 h incubation at room temperature, the samples were centrifuged at 13 500 rpm for 30 min. Finally, the supernatants were collected and analyzed by electrophoresis on the 0.8% agarose gels containing 0.01% Gelred (Beyotime Institute of Biotechnology, Beijing, China). The gels were photographed under ultraviolet light. The bands were analyzed using the FluorChem M fluorescent chemiluminescence imaging analysis system (Alpha Technologies, USA). The results were analyzed with SPSS version 17.0 (IBM, Chicago, IL, USA) using the two-tailed Student's *t*-test. A p-value ≤ 0.05 between groups was considered significant.

Conflicts of interest

There are no conflicts to declare.

Acknowledgements

We thank Seung-gu Kang, Tien Huynh and Xuanyu Meng for helpful discussions. This work was partially supported by the National Natural Science Foundation of China (Grant No. 11574224, 11404233, and 11374221) and the Natural Science Foundation of Jiangsu Province (Grant No. BK20161213). A Project Funded by the Priority Academic Program Development of Jiangsu Higher Education Institutions (PAPD), and the Jiangsu Provincial Key Laboratory of Radiation Medicine and Protection. RZ acknowledges the support from the IBM Blue Gene Science Program (W1258591, W1464125, and W1464164).

References

1 H. Bao, Y. Pan, Y. Ping, N. G. Sahoo, T. Wu, *et al.*, Chitosan-functionalized graphene oxide as a nanocarrier for drug and gene delivery, *Small*, 2011, **7**(11), 1569–1578.
2 L. Wang, Y. Wang, J. I. Wong, T. Palacios, J. Kong, *et al.*, Functionalized mos2 nanosheet-based field-effect biosensor for label-free sensitive detection of cancer marker proteins in solution, *Small*, 2014, **10**(6), 1101–1105.
3 C. Zhu, Z. Zeng, H. Li, F. Li, C. Fan, *et al.*, Single-layer mos2-based nanoprobes for homogeneous detection of biomolecules, *J. Am. Chem. Soc.*, 2013, **135**(16), 5998–6001.
4 Y. Shao, J. Wang, H. Wu, J. Liu, I. A. Aksay, *et al.*, Graphene based electrochemical sensors and biosensors: A review, *Electroanalysis*, 2010, **22**(10), 1027–1036.
5 B. Li, Y. Cheng, J. Liu, C. Yi, A. S. Brown, *et al.*, Direct optical imaging of graphene in vitro by nonlinear femtosecond laser spectral reshaping, *Nano Lett.*, 2012, **12**(11), 5936–5940.
6 Z. Yang, S.-G. Kang and R. Zhou, Nanomedicine: De novo design of nanodrugs, *Nanoscale*, 2014, **6**(2), 663–677.
7 K. Yang, J. Wan, S. Zhang, B. Tian, Y. Zhang, *et al.*, The influence of surface chemistry and size of nanoscale graphene oxide on photothermal therapy of cancer using ultra-low laser power, *Biomaterials*, 2012, **33**(7), 2206–2214.
8 M. Li, X. Yang, J. Ren, K. Qu and X. Qu, Using graphene oxide high near-infrared absorbance for photothermal

treatment of alzheimer's disease, *Adv. Mater.*, 2012, **24**(13), 1722–1728.

9 C. Ge, J. Du, L. Zhao, L. Wang, Y. Liu, *et al.*, Binding of blood proteins to carbon nanotubes reduces cytotoxicity, *Proc. Natl. Acad. Sci. U. S. A.*, 2011, **108**(41), 16968–16973.

10 B. Luan, T. Huynh, L. Zhao and R. Zhou, Potential toxicity of graphene to cell functions via disrupting protein-protein interactions, *ACS Nano*, 2015, **9**(1), 663–669.

11 S. G. Kang, G. Zhou, P. Yang, Y. Liu, B. Sun, *et al.*, Molecular mechanism of pancreatic tumor metastasis inhibition by gd@c82(oh)22 and its implication for de novo design of nanomedicine, *Proc. Natl. Acad. Sci. U. S. A.*, 2012, **109**(38), 15431–15436.

12 Y. Tu, M. Lv, P. Xiu, T. Huynh, M. Zhang, *et al.*, Destructive extraction of phospholipids from escherichia coli membranes by graphene nanosheets, *Nat. Nanotechnol.*, 2013, **8**(8), 594–601.

13 M. Mathesh, B. Luan, T. O. Akanbi, J. K. Weber, J. Liu, *et al.*, Opening lids: Modulation of lipase immobilization by graphene oxides, *ACS Catal.*, 2016, **6**(7), 4760–4768.

14 S. He, B. Song, D. Li, C. Zhu, W. Qi, *et al.*, A graphene nanoprobe for rapid, sensitive, and multicolor fluorescent DNA analysis, *Adv. Funct. Mater.*, 2010, **20**(3), 453–459.

15 A. Chen and C. Ostrom, Palladium-based nanomaterials: Synthesis and electrochemical applications, *Chem. Rev.*, 2015, **115**(21), 11999–12044.

16 A. J. McGrath, Y.-H. Chien, S. Cheong, D. A. J. Herman, J. Watt, *et al.*, Gold over branched palladium nano structures for photothermal cancer therapy, *ACS Nano*, 2015, **9**(12), 12283–12291.

17 R. Long, K. Mao, X. Ye, W. Yan, Y. Huang, *et al.*, Surface facet of palladium nanocrystals: A key parameter to the activation of molecular oxygen for organic catalysis and cancer treatment, *J. Am. Chem. Soc.*, 2013, **135**(8), 3200–3207.

18 C. P. Adams, K. A. Walker, S. O. Obare and K. M. Docherty, Size-dependent antimicrobial effects of novel palladium nanoparticles, *PLoS One*, 2014, **9**(1), e85981.

19 H. Heinz, B. L. Farmer, R. B. Pandey, J. M. Slocik, S. S. Patnaik, *et al.*, Nature of molecular interactions of peptides with gold, palladium, and pd-au bimetal surfaces in aqueous solution, *J. Am. Chem. Soc.*, 2009, **131**(28), 9704–9714.

20 Z. Yang, Z. Wang, X. Tian, P. Xiu and R. Zhou, Amino acid analogues bind to carbon nanotube via pi-pi interactions: Comparison of molecular mechanical and quantum mechanical calculations, *J. Chem. Phys.*, 2012, **136**(2), 025103.

21 Z. L. Gu, Z. X. Yang, L. L. Wang, H. Zhou, C. A. Jimenez-Cruz, *et al.*, The role of basic residues in the adsorption of blood proteins onto the graphene surface, *Sci. Rep.*, 2015, **5**, 10873.

22 Z. Gu, Z. Yang, Y. Chong, C. Ge, J. K. Weber, *et al.*, Surface curvature relation to protein adsorption for carbon-based nanomaterials, *Sci. Rep.*, 2015, **5**, 10886.

23 Z. Xu, Y. Gao, C. L. Wang and H. P. Fang, Nanoscale hydrophilicity on metal surfaces at room temperature: Coupling lattice constants and crystal faces, *J. Phys. Chem. C*, 2015, **119**(35), 20409–20415.

24 L. B. Wright, J. P. Palafox-Hernandez, P. M. Rodger, S. Corni and T. R. Walsh, Facet selectivity in gold binding peptides: Exploiting interfacial water structure, *Chem. Sci.*, 2015, **6**(9), 5204–5214.

25 Z. E. Hughes, R. Kochandra and T. R. Walsh, Facet-specific adsorption of tripeptides at aqueous au interfaces: Open questions in reconciling experiment and simulation, *Langmuir*, 2017, **33**(15), 3742–3754.

26 I. L. Geada, H. Ramezani-Dakhel, T. Jamil, M. Sulpizi and H. Heinz, Insight into induced charges at metal surfaces and biointerfaces using a polarizable lennard-jones potential, *Nat. Commun.*, 2018, **9**, 716.

27 F. Tavanti, A. Pedone, P. Matteini and M. C. Menziani, Computational insight into the interaction of cytochrome c with wet and pvp-coated ag surfaces, *J. Phys. Chem. B*, 2017, **121**(41), 9532–9540.

28 H. Ramezani-Dakhel, L. Ruan, Y. Huang and H. Heinz, Molecular mechanism of specific recognition of cubic pt nanocrystals by peptides and of the concentration-dependent formation from seed crystals, *Adv. Funct. Mater.*, 2015, **25**(9), 1374–1384.

29 C. Ge, G. Fang, X. Shen, Y. Chong, W. G. Wamer, *et al.*, Facet energy versus enzyme-like activities: The unexpected protection of palladium nanocrystals against oxidative damage, *ACS Nano*, 2016, **10**(11), 10436–10445.

30 T. Cedervall, I. Lynch, S. Lindman, T. Berggard, E. Thulin, *et al.*, Understanding the nanoparticle-protein corona using methods to quantify exchange rates and affinities of proteins for nanoparticles, *Proc. Natl. Acad. Sci. U. S. A.*, 2007, **104**(7), 2050–2055.

31 M. P. Monopoli, C. Åberg, A. Salvati and K. A. Dawson, Biomolecular coronas provide the biological identity of nanosized materials, *Nat. Nanotechnol.*, 2012, **7**(12), 779.

32 P. Del Pino, B. Pelaz, Q. Zhang, P. Maffre, G. U. Nienhaus, *et al.*, Protein corona formation around nanoparticles - from the past to the future, *Mater. Horiz.*, 2014, **1**(3), 301–313.

33 V. Castagnola, W. Zhao, L. Boselli, M. C. Lo Giudice, F. Meder, *et al.*, Biological recognition of graphene nanoflakes, *Nat. Commun.*, 2018, **9**, 1577.

34 I. Chakraborty, N. Feliu, S. Roy, K. Dawson and W. J. Parak, Protein-mediated shape control of silver nanoparticles, *Bioconjugate Chem.*, 2018, **29**(4), 1261–1265.

35 X. Ma, J. Huh, W. Park, L. P. Lee, Y. J. Kwon, *et al.*, Gold nanocrystals with DNA-directed morphologies, *Nat. Commun.*, 2016, **7**, 12873.

36 L. H. Tan, Y. Yue, N. S. R. Satyavolu, A. S. Ali, Z. D. Wang, *et al.*, Mechanistic insight into DNA-guided control of

nanoparticle morphologies, *J. Am. Chem. Soc.*, 2015, **137**(45), 14456–14464.
37 N. S. R. Satyavolu, L. H. Tan and Y. Lu, DNA-mediated morphological control of pd-au bimetallic nanoparticles, *J. Am. Chem. Soc.*, 2016, **138**(50), 16542–16548.
38 J. J. X. Wu, L. H. Tan, K. Hwang, H. Xing, P. W. Wu, *et al.*, DNA sequence-dependent morphological evolution of silver nanoparticles and their optical and hybridization properties, *J. Am. Chem. Soc.*, 2014, **136**(43), 15195–15202.
39 C. Y. Chiu, H. Wu, Z. Y. Yao, F. Zhou, H. Zhang, *et al.*, Facet-selective adsorption on noble metal crystals guided by electrostatic potential surfaces of aromatic molecules, *J. Am. Chem. Soc.*, 2013, **135**(41), 15489–15500.
40 H. E. Lee, H. Y. Ahn, J. Mun, Y. Y. Lee, M. Kim, *et al.*, Amino-acid- and peptide-directed synthesis of chiral plasmonic gold nanoparticles, *Nature*, 2018, **556**(7701), 360–365.
41 Z. Gu, Y. Zhang, B. Luan and R. Zhou, DNA translocation through single-layer boron nitride nanopores, *Soft Matter*, 2016, **12**(3), 817–823.
42 B. Hess, C. Kutzner, D. van der Spoel and E. Lindahl, Gromacs 4: Algorithms for highly efficient, load-balanced, and scalable molecular simulation, *J. Chem. Theory Comput.*, 2008, **4**(3), 435–447.
43 A. D. Mackerell, M. Feig and C. L. Brooks, Extending the treatment of backbone energetics in protein force fields: Limitations of gas-phase quantum mechanics in reproducing protein conformational distributions in molecular dynamics simulations, *J. Comput. Chem.*, 2004, **25**(11), 1400–1415.
44 A. D. MacKerell, D. Bashford, M. Bellott, R. L. Dunbrack, J. D. Evanseck, *et al.*, All-atom empirical potential for molecular modeling and dynamics studies of proteins, *J. Phys. Chem. B*, 1998, **102**(18), 3586–3616.
45 H. Heinz, R. A. Vaia, B. L. Farmer and R. R. Naik, Accurate simulation of surfaces and interfaces of face-centered cubic metals using 12-6 and 9-6 lennard-jones potentials, *J. Phys. Chem. C*, 2008, **112**(44), 17281–17290.
46 W. Humphrey, A. Dalke and K. Schulten, Vmd: Visual molecular dynamics, *J. Mol. Graphics Modell.*, 1996, **14**(1), 33–38.
47 W. L. Jorgensen, J. Chandrasekhar, J. D. Madura, R. W. Impey and M. L. Klein, Comparison of simple potential functions for simulating liquid water, *J. Chem. Phys.*, 1983, **79**(2), 926–935.
48 G. Bussi, D. Donadio and M. Parrinello, Canonical sampling through velocity rescaling, *J. Chem. Phys.*, 2007, **126**(1), 014101.
49 H. J. C. Berendsen, J. P. M. Postma, W. F. Vangunsteren, A. Dinola and J. R. Haak, Molecular-dynamics with coupling to an external bath, *J. Chem. Phys.*, 1984, **81**(8), 3684–3690.
50 U. Essmann, L. Perera, M. L. Berkowitz, T. Darden, H. Lee, *et al.*, A smooth particle mesh ewald method, *J. Chem. Phys.*, 1995, **103**(19), 8577–8593.
51 T. Darden, D. York and L. Pedersen, Particle mesh ewald - an n.Log(n) method for ewald sums in large systems, *J. Chem. Phys.*, 1993, **98**(12), 10089–10092.
52 B. Hess, H. Bekker, H. J. C. Berendsen and J. Fraaije, Lincs: A linear constraint solver for molecular simulations, *J. Comput. Chem.*, 1997, **18**(12), 1463–1472.
53 B. Hess, P-lincs: A parallel linear constraint solver for molecular simulation, *J. Chem. Theory Comput.*, 2008, **4**(1), 116–122.
54 M. J. Abraham, T. Murtola, R. Schulz, S. Páll, J. C. Smith, *et al.*, Gromacs: High performance molecular simulations through multi-level parallelism from laptops to supercomputers, *SoftwareX*, 2015, **1–2**, 19–25.
55 P. W. Fowler, K. H. Tai and M. S. P. Sansom, The selectivity of k + ion channels: Testing the hypotheses, *Biophys. J.*, 2008, **95**(11), 5062–5072.
56 B. I. Costescu and F. Grater, Time-resolved force distribution analysis, *BMC Biophys.*, 2013, **6**(1), 5.
57 H. Poulsen, P. Nissen, O. G. Mouritsen and H. Khandelia, Protein kinase a (pka) phosphorylation of na+/k+-atpase opens intracellular c-terminal water pathway leading to third na+-binding site in molecular dynamics simulations, *J. Biol. Chem.*, 2012, **287**(19), 15959–15965.
58 W. Yuan, W. F. Li, Y. G. Mu and M. B. Chan-Park, Effect of side-chain structure of rigid polyimide dispersant on mechanical properties of single-walled carbon nanotube/cyanate ester composite, *ACS Appl. Mater. Interfaces*, 2011, **3**(5), 1702–1712.
59 J. Yoo and A. Aksimentiev, Competitive binding of cations to duplex DNA revealed through molecular dynamics simulations, *J. Phys. Chem. B*, 2012, **116**(43), 12946–12954.
60 S. Miyamoto and P. A. Kollman, Settle - an analytical version of the shake and rattle algorithm for rigid water models, *J. Comput. Chem.*, 1992, **13**(8), 952–962.
61 S. Kumar, J. M. Rosenberg, D. Bouzida, R. H. Swendsen and P. A. Kollman, Multidimensional free-energy calculations using the weighted histogram analysis method, *J. Comput. Chem.*, 1995, **16**(11), 1339–1350.
62 G. M. Torrie and J. P. Valleau, Non-physical sampling distributions in monte-carlo free-energy estimation - umbrella sampling, *J. Comput. Phys.*, 1977, **23**(2), 187–199.
63 B. Roux, The calculation of the potential of mean force using computer-simulations, *Comput. Phys. Commun.*, 1995, **91**(1–3), 275–282.
64 J. S. Hub, B. L. de Groot and D. van der Spoel, G_wham-a free weighted histogram analysis implementation including robust error and autocorrelation estimates, *J. Chem. Theory Comput.*, 2010, **6**(12), 3713–3720.
65 J. G. Kirkwood, Statistical mechanics of fluid mixtures, *J. Chem. Phys.*, 1935, **3**(5), 300–313.
66 B. Efron, 1977 rietz lecture - bootstrap methods - another look at the jackknife, *Ann. Stat.*, 1979, **7**(1), 1–26.
67 L. Zhao, J. Xu, Y. Yang, Y. Chong, C. Liu, *et al.*, Inhibitory impacts of chemically modified tetracycline-3 and underlying mechanism in human cervical cancer cells, *Anti-Cancer Drugs*, 2013, **24**(8), 799–809.

